Journal of Catalysis 412 (2022) 78–86

Contents lists available at ScienceDirect

Journal of Catalysis

journal homepage: www.elsevier.com/locate/jcat

Metal coordination determines the catalytic activity of IrO_2 nanoparticles for the oxygen evolution reaction

Danilo González, Mariona Sodupe, Luis Rodríguez-Santiago, Xavier Solans-Monfort *

Departament de Química, Universitat Autònoma de Barcelona, 08193 Bellaterra, Spain

ARTICLE INFO

Article history:
Received 14 February 2022
Revised 10 May 2022
Accepted 31 May 2022
Available online 4 June 2022

Keywords:
Water electrolysis
Oxygen Evolution Reaction
Iridium oxide
Nanoparticles
DFT

ABSTRACT

H_2 production through water electrolysis is a promising strategy for storing sunlight energy. For the oxygen evolution reaction, iridium oxide containing materials are state-of-the-art due to their stability in acidic conditions. Moreover, precious metal content can be reduced by using small nanoparticles that show high catalytic activities. We performed DFT calculations on a 1.2 nm large IrO_2 Wulff-like stoichiometric nanoparticle model (IrO_2) with the aim of determining the factors controlling the catalytic activity of IrO_2 nanoparticles. Results show that at reaction conditions tetra- and tricoordinated iridium centers are not fully oxidized, the major species being IrO(OH) and $IrO(OH)_2$, respectively. Although the computed overpotential show that all centers present relatively similar reactivities, low coordinated iridium centers tend to be more active than the pentacoordinates sites of the well-defined facets. These low coordination sites are likely more abundant on amorphous nanoparticles, which could be one of the factors explaining the higher catalytic activity observed for non-crystalline materials.

1. Introduction

The use of H_2 as sunlight energy storing source is seen as one of the most promising strategies for obtaining clean energy.[1,2] This can be achieved through the (photo)electrochemical splitting of water that converts water in oxygen at the anode through the oxygen evolution reaction (OER) and H_2 at the cathode by means of the hydrogen evolution reaction (HER).[3–9] The OER is a four-electron process that presents high overpotentials and slow kinetics and is considered the limiting half reaction for the application of water electrolysis as source for sustainable energy conversion and storage.[10–12] Several OER promising catalysts have been reported in the literature.[13,14] Within the large list of catalytically active species, IrO_2 is considered to be the most efficient one in acidic media due to both its catalytic activity and stability in harsh reaction conditions.[11,12,15].

Iridium is an expensive precious metal and consequently lowering the iridium content on the catalyst is an essential issue for the practical implementation of the water splitting.[15–20] Several research groups have synthetized small $IrO_2(IrO_X)$ nanoparticles of different sizes and shapes showing intrinsic activities that are slightly higher than with crystalline films. Such improved intrinsic activity becomes remarkably high when normalizing by the catalyst amount[21–33] Indeed, nanoparticles of about 1.5 – 2.0 nm have been shown to be within the most active species, [21,26,29,32,33] the origin of their high activity being associated to three factors: i) the Ir(III)/Ir(IV) ratio; ii) the amount of surface hydroxylated species and iii) the degree of amorphization.

Three main reaction mechanisms have been proposed for the OER (Scheme 1):[10,11,34–37] i) the water nucleophilic attack (WNA) in which the O-O bond of O_2 is formed by the reaction of an Ir=O species of the surface and a water molecule of the solution; ii) the oxo-coupling mechanism (I2M) in which the O-O bond is formed by the coupling of two Ir=O species on the surface and iii) the lattice oxygen evolution reaction mechanism (LOER) that involve oxygen atoms from the material in the O_2 formation. Isotope labeling experiments showed that the LOER mechanism is important in amorphous materials but does not contribute in crystalline rutile-like materials.[11,38] Based on that, we decided not to consider the LOER pathway in the present contribution, since our models (see below) are constructed from crystalline IrO_2. Indeed, for crystalline IrO_2, the WNA pathway is the most accepted mechanism, except in very flexible environments, where the I2M mechanism becomes competitive.[39,40] Remarkably, the local morphology of the material seems to tune the catalytic activity of IrO_2 for OER.[41–44].

From a computational point of view, the catalytic activity of iridium-based materials for the OER has been addressed either with slab models of the (110) surface[39,45–56] or small clusters up to 13 Ir centers.[57,58] Regarding the studies with slab models,

* Corresponding author at: Departament de Química, Universitat Autònoma de Barcelona, Carrer dels Til·lers s/n, 08193 Bellaterra, Spain.
E-mail address: xavier.solans@uab.cat (X. Solans-Monfort).

https://doi.org/10.1016/j.jcat.2022.05.023
0021-9517/

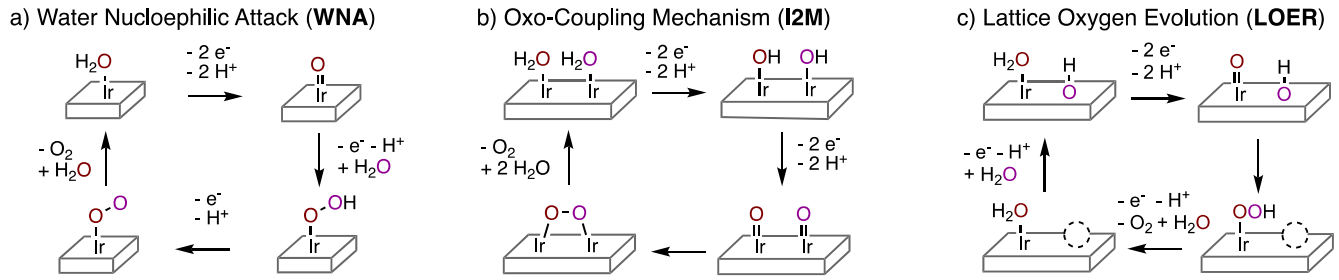

Scheme 1. Reaction mechanisms for the oxygen evolution reaction proposed in the literature.

most contributions limit the study to the thermodynamic cost of each PCET step. Only in a few cases, the energy barriers associated with some of the elementary steps have been computed (mostly the chemical ones) and the associated energy barriers tend to be low,[47,48,52,53,56] thus suggesting that the thermodynamics of the PCET is sufficient to get overpotential trends. Moreover, while most of these contributions agree that the most favorable mechanism on the (110) surface is the WNA, some discrepancies exist on the nature of the overpotential defining step. Indeed, three different steps have been proposed to be rate limiting depending on the level of theory used and the definition of the elementary steps of the reaction: i) the Ir-OH to Ir-O oxidation; ii) the electrochemical step associated with the Ir-OOH intermediate formation and iii) the O_2 release. On the other hand, regarding the OER on cluster models, Auer and co-workers analyzed the effect of the applied potential and pH on the structure of two models containing either 3 or 13 iridium centers.[58] Results for the larger cluster show that at acidic reaction conditions the surface presents mainly Ir-O and Ir-OH groups, the number of Ir-OH decreasing when increasing the applied potential and the pH. Moreover, the O-O bond formation through the WNA mechanism is predicted to present a non-negligible energy barrier that decreases while increasing the applied potential.

Remarkably, nanoparticles, even being crystalline, present particular sites such as tips, edges and corners whose representation with extended models may not be appropriate, even if other surfaces other than the (1 1 0) are taken into account.[48] In addition, clusters may not properly represent the electronic structure of the commonly used nanoparticle sizes. In this contribution, we address the OER reaction on all potentially active sites present in the stoichiometric Wulff-like $(IrO_2)_{33}$ nanoparticle model. Results show that although the reactivity of all considered sites is relatively similar, the oxygen evolution reaction on tri- and tetracoordinated iridium centers tends to present lower overpotentials than on pentacoordinated sites. This is associated with the presence of $Ir(OH)_n$ species at reaction conditions. These low coordinated sites are likely more abundant in amorphous materials, thereby providing a plausible explanation on the high catalytic activity of non-crystalline IrO_2 and its dependence with the presence of $Ir(OH)_n$ species on the surface.

2. Computational details

A Wulff-like stoichiometric nanoparticle model of 1.2 nm size was constructed with the BCN-M computational tool (Fig. 1).[59] The surface energies provided to construct the model are 0.150, 0.158, 0.185 and 0.206 eV A^{-2} for the (1 1 0), (0 1 1), (1 0 0) and (0 0 1) crystallographic surfaces,[60] respectively. The final model contains 33 IrO_2 units, its size is close to some of the experimentally reported active nanoparticles,[21,26,29,32,33] and it is computationally affordable. Remarkably, the full optimization of $Ir_{33}O_{66}$ in vacuum implied an important reconstruction around

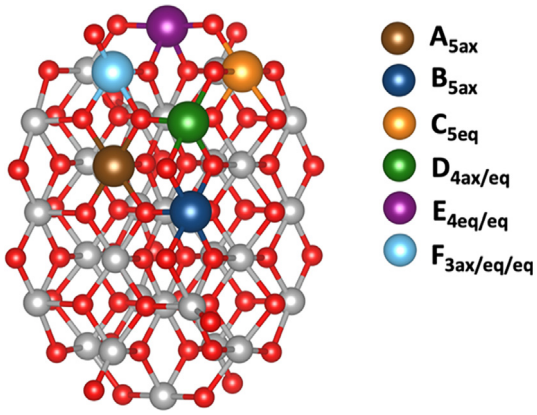

Fig. 1. $(IrO_2)_{33}$ nanoparticle model with the undercoordinated iridium centers (coloured atoms) where OER activity has been studied.

the tip site. This reconstruction implies the breaking of Ir-O bonds and the formation of Ir-Ir interactions as described previously.[61] However, since IrO_X nanoparticles are experimentally synthetized in water solution, it is very likely that the reconstruction observed in vacuum does not represent the experimental structure. With the aim of better describing the aqueous environment in which IrO_2 nanoparticles are usually synthetized, we constructed a model including a water molecule in each surface iridium vacant site. The full optimization of this model lead to some surface relaxation but the reconstruction around the tip was prevented. After full optimization, the added water molecules were removed, and all nanoparticle atoms, except the singly coordinated oxygen atoms, were kept fix in all subsequent calculations.

At reaction conditions, it is expected that the nanoparticle would be highly oxidized, thus presenting several Ir-OH and Ir=O groups at the vacant sites of the surface iridium atoms. Inclusion of these groups in each iridium center in combination with the spin polarized formalism makes SCF convergence more time consuming. Moreover, determining the surface termination at 1.5 V potentials including explicitly the 38 water molecules and analyzing all potential PCET associated to these water molecules is prohibitive. In this context, we decided to use a model where we only considered the oxidation of water molecules located at adjacent iridium centers, with the final goal of having two Ir-O centers to carry on the reaction. One of the two Ir-O centers acts as the active site and the neighbor one either actively participate in the oxo-coupling mechanism or it assists the chemical water nucleophilic attack step. In addition, we constructed a second model in which all surface iridium centers are oxidized to the most stable structure at 1.5 V (according to the results obtained with the first model). This model was used to analyze how the imposed constraints associated to the partial optimization and the degree of oxidation of the nanoparticle influences the reactivity of the **A_{5ax}-A_{5ax}** site. That is, with the fully oxidized model we computed the energetics of the

WNA mechanism assuming two approaches. In the first one the nanoparticle was kept fixed as in the partial oxidized model and in the second one the nanoparticle was fully optimized. That is, comparison between the three models, partial oxidation with constrained optimization, full oxidation with constrained optimization and full optimization of the oxidized model allows distinguishing the effects arising from the degree of oxidation of the nanoparticle and the effects of the constrained optimization. Results are shown in Table S1 of the supplementary materials, where we also added the data for the fully optimized (1 1 0) surface considering two supercell models, one fully oxidized $(1\,1\,0)_{2x1}$ and one half oxidized $(1\,1\,0)_{2x2}$. Results show that the degree of oxidation of the neighbor iridium centers has very little influence on the overall overpotential. However, the effect of relaxing the geometry constraints is more pronounced, the overpotential decreasing by about 0.20–0.25 V. All PCET steps become easier and close to the results with the surface models. Indeed, according to the results provided below, it is very likely that slab models of the sites existing on the surface may lead to similar results to those obtained for the realistic nanoparticle model. The decrease of the PCET reaction energies is associated to a relative stabilization of the most oxidized species with respect to the less oxidized ones that may be related with the fact that the restricted structure corresponds to that in which water is adsorbed on each vacant site, i.e. the structure of the less oxidized species. A similar effect should be expected with the other sites, but due to the limitations of the model, small difference between sites should be taken with care.

All calculations were performed with the VASP code,[62,63] using the spin polarized formalism, the PBE density functional [64] and the Grimme's D2 empirical correction to account for dispersion forces.[65] PBE functional has been widely used in modeling the OER with iridium based materials including finite clusters [39,40,48,52,53,55,58] and according to Goddard and co-workers represents the metallic nonmagnetic electronic structure of the bulk in better agreement with experiments than hybrid functionals or the PBE-U approach.[66] Unfortunately, it is also well known that GGA functionals tends to delocalize the electron density of unpaired electrons[67] as it is the case of the Ir-O oxo species. To ensure that the electron delocalization has no effect on the O-O bond formation step, we performed selected calculations with the PBE + U approach. As shown in Table S2, inclusion of the Hubbard term marginally increases the spin density on the oxyl species of the IrO_2 (1 1 0) main surface and this makes the I2M mechanism slightly less unfavorable. However, the WNA mechanism is always preferred by at least 1.0 eV. PAW pseudopotentials were used to describe the ionic cores.[68,69] The valence electrons were represented with a plane wave basis with a kinetic energy cutoff of 500 eV. Moreover, single point calculations at the final optimized geometries were performed to include solvent effects (water, ε = 80.0) with VASPsol package.[70] It has been recently shown[71] that the inclusion of solvent through implicit solvent models does not necessarily leads to a better description of adsorbed species related to electrocatalysis such as OH or OOH. Therefore, we decided to compare the results with and without implicit solvation (Table S3 of the supplementary materials). Inclusion of solvent through an implicit model has a non-negligible effect on processes involving the adsorption of water, but it has small effect on the energetics of the proton coupled electron transfer steps (PCET). Consequently, the main trends are preserved both with and without the inclusion of implicit solvent. The nanoparticle model was placed in a cubic box of a 30 Å edge and the calculations were performed at gamma point due to the model dimensionality.

Since the global process has been experimentally determined to be endothermic by 4.92 eV and it implies four PCET, an ideal electrocatalyst should catalyze these reactions at potentials of 1.23 V. Therefore, the minimum required overpotential (η^{OER}) is computed as the ΔG° difference between the highest in Gibbs energy PCET process and 1.23 V and it is used to identify the most active sites. Note that the reaction energy is imposed to be 4.92 eV due to the way the G° of O_2 is computed (see below).

$$\eta^{OER} = \max[\Delta G\circ\,(PCET)]/e^- - 1.23 \quad (1)$$

Values reported along the text are based on Gibbs energies at 1 atm and T = 273.15 K assuming the computational standard hydrogen electrode for the proton coupled electron transfer steps (PCET).[45,72] Thermal contributions were computed through different approximations: i) For the OER intermediates, the thermal corrections were obtained by considering the contributions to the vibrational modes of the adsorbed species and the Ir-O_{ads} stretching mode. This is 6, 3, 1, 5 and 3 vibrational modes per adsorbed $^*H_2O$, $^*OH$, $^*O$, $^*OOH$ and $^*OO$ species, respectively; ii) The entropy term of H_2O and H_2 were taken from tabulated values for liquid H_2O and H_2 gas, respectively; and iii) In analogy with previous contributions,[39,45,53] the O_2 Gibbs energy (in eV) was computed as $4.92 + 2\,G^0_{H2O} - 2G^0_{H2}$ where 4.92 is the experimental reaction energy and G^0_{H2O} and $2G^0_{H2}$ are the computed Gibbs energies for water and hydrogen, respectively.

3. Results and discusion

We have studied the catalytic activity for the oxygen evolution reaction of the six different undercoordinated iridium centers present in the $(IrO_2)_{33}$ nanoparticle (Fig. 1): $\mathbf{A_{5ax}}$ (brown), $\mathbf{B_{5ax}}$ (dark blue), $\mathbf{C_{5eq}}$ (orange), $\mathbf{D_{4ax/eq}}$ (green), $\mathbf{E_{4eq/eq}}$ (purple) and $\mathbf{F_{3ax/eq/eq}}$ (light blue). We have only considered the I2M and WNA proposed mechanisms since our nanoparticle model is based on the crystalline material, for which the LOER reaction mechanism (Scheme 1c) has been reported to be non-operative. The six centers differ on the coordination number and environment. Taking into account that iridium in rutile shows two short Ir-O axial distances and four long equatorial ones,[60] the six centers can be divided in five different types: i) pentacoordinated atoms with an axial vacant site ($\mathbf{A_{5ax}}$ and $\mathbf{B_{5ax}}$); ii) pentacoordinated sites with an equatorial vacancy ($\mathbf{C_{5eq}}$); iii) tetracoordinated centers with one axial and one equatorial vacant site ($\mathbf{D_{4ax/eq}}$); iv) tetracoordinated sites with two equatorial vacant sites ($\mathbf{E_{4eq/eq}}$); and v) iridium centers presenting only three bonds with lattice oxygens ($\mathbf{F_{3ax/eq/eq}}$). While other sites exist in larger Wulff-like nanoparticle models, they can all be classified in one of these five types of centers.[59,61] Indeed, we found that the water adsorption in the existing sites of $(IrO_2)_{33}$ and $(IrO_2)_{115}$ nanoparticle models is mainly determined by the nature of the vacant site and nanoparticle morphology and not by the nanoparticle size.[61] Therefore, the results reported here should be indicative of how the different sites of the nanoparticle react.

The results and discussion section is organized in two parts. We first focus on the oxidation of the surface iridium centers in the presence of water as a function of the applied potential[61] and afterwards, we explore the OER reaction starting from the most stable species at 1.5 V, through either the I2M and WNA mechanisms. The choice for 1.5 V is based on the fact that this potential is close to the optimal value for performing the OER reaction with different Ir-based materials.[26,53,73].

3.1. Oxidation of surface Ir-$(H_2O)_X$

The oxidation of the six iridium centers of $(IrO_2)_{33}$ model (Fig. 1) in the presence of water as a function of the applied potential has been analyzed with the aim of establishing the most stable structure at potentials around 1.5 V. Since we considered both the

I2M and WNA mechanisms and the former path requires the participation of two Ir-O groups, the active site oxidation was modeled by considering either one single center that could lead to the formation of two oxo groups ($\mathbf{D_{4ax/eq}}$, $\mathbf{E_{4eq/eq}}$ or $\mathbf{F_{3ax/eq/eq}}$) or two vicinal iridium centers ($\mathbf{A_{5ax}}$-$\mathbf{A_{5ax}}$, $\mathbf{D_{4ax/eq}}$-$\mathbf{B_{5ax}}$, $\mathbf{D_{4ax/eq}}$-$\mathbf{C_{eq}}$, $\mathbf{F_{3ax/eq/eq}}$-$\mathbf{A_{5ax}}$or $\mathbf{F_{3ax/eq/eq}}$-$\mathbf{D_{4ax/eq}}$). The oxidation process takes place through several proton coupled electron transfer steps (PCET) and transforms the adsorbed water molecules to either Ir-OH or Ir-O species. The initial structure arises from adding one water molecule per vacant site in its preferred form (molecular or dissociated) as discussed in our previous contribution.[61] Then, we considered the PCET processes until all metal centers present Ir-O species only. We explored all possibilities for the individual tri- and tetracoordinated sites and for systems involving two centers the combinations of the most stable structures of each site only. The optimized structures of the most stable isomers involved in the surface oxidation (Figures S1 to S8), the relative Gibbs energies between the different isomers of the intermediates involved in the oxidation process and the reaction Gibbs energies for all steps (Tables S4 to S18) are reported in the supplementary material.

Relative stabilities of the different species as a function of the applied potential were computed following equation (2).

$$\mathbf{X(H_2O)\text{-}Y(H_2O)} \rightarrow \mathbf{X(L_1)\text{-}Y(L_2)} + ne^- + nH^+$$
$$\Delta G^0 = G^0_{L1/L2} - G^0_{H2O/H2O} - nU. \quad (2)$$

where $\mathbf{X(L_1)\text{-}Y(L_2)}$ stands for the oxidized species arising from $\mathbf{X(H_2O)\text{-}Y(H_2O)}$, n is the number of PCET processes required to go from $\mathbf{X(H_2O)\text{-}Y(H_2O)}$ to $\mathbf{X(L_1)\text{-}Y(L_2)}$ and U is the applied potential. Fig. 2 summarizes the results. The color labeling indicates the most oxidized species in each center: i) grey indicates that all vacant sites are occupied by molecular or dissociated water molecules; ii) the green color indicates that at least one OH group as most oxidized species is present in one of the two considered centers; iii) the blue series accounts for structures with at least one OH group as the most oxidized species at each iridium site; iv) orange color describes species with one Ir-O group in one of the metal centers and; v) the pink colors indicate the presence of two Ir-O species (Scheme 2). According to our results on surface models,[48] the oxygen evolution catalysis requires the formation of species represented in pink in Fig. 2, at around 1.5 V potentials.

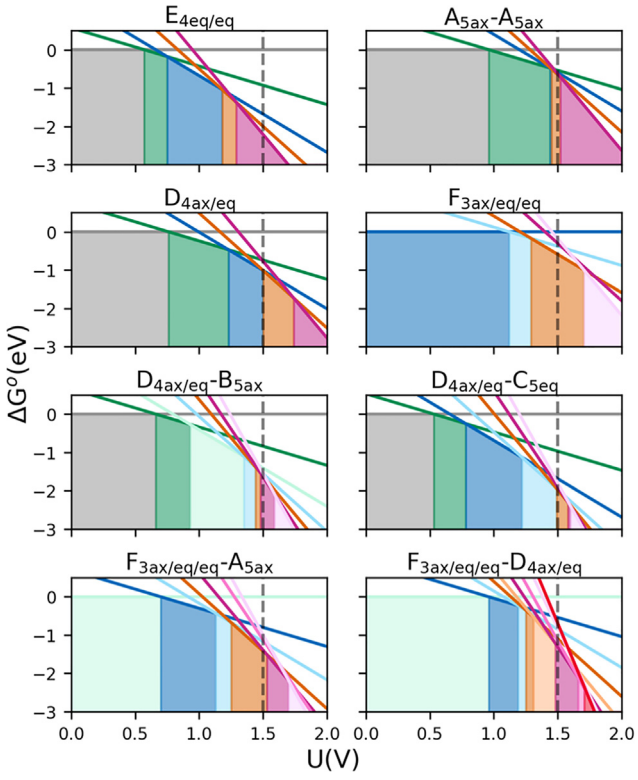

Fig. 2. Phase diagram of the different sites of $(IrO_2)_{33}$ at pH = 0, T = 298 K and P = 1 atm as a function of the applied potential. Color labeling according to Scheme 2.

Results show that the required potential for the H_2O to OH oxidation is sensitive to the neighbor metal that is also being oxidized. The computed potentials for the H_2O to OH oxidation for one specific center can vary up to 0.2 eV and this appears to be related with the formation of hydrogen bonds. Centers able to establish strong hydrogen bonds with neighbor adsorbed species tend to present higher potentials for the H_2O to OH oxidation. However, this difference will likely be smaller if explicit solvent water molecules are added in the simulation due to the formation of hydrogen bonds between the adsorbed species and the solvent. Moreover, the H_2O to OH transition always takes place at low potentials and thus, this oxidation step does not appear to play a key role in the OER with iridium-based metals.

The Ir-OH to Ir-O oxidation is much less sensitive to the neighbor iridium center that it is being oxidized and this is related with the fact that Ir-OH species do not form strong hydrogen bonding with species adsorbed in the vicinity. Consequently, the values for each iridium center are essentially not affected by the nature of the other metal that is being oxidized (less than 0.08 eV). The formation of the first Ir-O species at tri- and tetracoordinated iridium centers occurs at potentials between 1.18 and 1.50 V and the computed values tend to be lower than the required potentials for oxidizing pentacoordinated centers (between 1.45 and 1.54 V). Despite these small differences may be sensitive to the modeling approach, the general trend of the required potential for the formation of the first Ir-O species follows the order $\mathbf{E_{4eq/eq}} < \mathbf{F_{3ax/eq/eq}} < \mathbf{D_{4ax/eq}} < \mathbf{A_{5ax}} \sim \mathbf{B_{5ax}} < \mathbf{C_{5eq}}$ and this agrees with the observed trends for extended surface models.[48] Remarkably, the Ir-OH to Ir-O oxidation of the equatorial and axial sites of $\mathbf{D_{4ax/eq}}$ with the other vacancy containing a Ir-OH group occurs at very similar potentials (difference of less than 0.03 V) and thus, both $\mathbf{D_{4eq/ax}(O/OH)}$ and $\mathbf{D_{4eq/ax}(OH/O)}$ structures should coexist.

Full oxidation of the tri- and tetracoordinated iridium centers ($\mathbf{D_{4eq/ax}}$, $\mathbf{F_{3ax/eq/eq}}$) requires high potentials (over 1.6 V). This suggests that at reaction conditions these centers will not be fully oxidized and they will remain as $Ir(O)(OH)_x$ (x = 1 or 2 for $\mathbf{D_{4eq/ax}}$ and $\mathbf{F_{3ax/eq/eq}}$ sites, respectively). $\mathbf{E_{4eq/eq}}$ located at the tip of the nanoparticle is an exception. According to calculations, the full oxidation of this center occurs at 1.29 V and thus, it will present two Ir-O groups in one single iridium atom at reaction conditions as already found for the analogous centers of the (001) surface and when using a slab model of the tip site ($\mathbf{E_{4eq/eq\text{-}slab}}$, Figure S9).[48] Overall, at 1.5 V the most stable structures for all considered systems are: $\mathbf{D_{4ax/eq}(OH/O)}$, $\mathbf{E_{4eq/eq}(O/O)}$, $\mathbf{F_{3ax/eq/eq}(O/OH/OH)}$, $\mathbf{A_{5ax}(O)\text{-}A_{5ax}(O)}$, $\mathbf{D_{4ax/eq}(OH/O)\text{-}B_{5ax}(O)}$, $\mathbf{D_{4ax/eq}(OH/O)\text{-}C_{5eq}(O)}$, $\mathbf{F_{3ax/eq/eq}(O/OH/OH)\text{-}A_{5ax}(O)}$ or $\mathbf{F_{3ax/eq/eq}(O/OH/OH)\text{-}D_{4ax/eq}(OH/O)}$.

3.2. Oxygen evolution reaction catalytic activity

In a second step, we studied the OER reaction starting from the most stable structure at potentials around 1.5 V. We performed the study in the pairs of sites having two Ir-O groups on the surface. We also considered $\mathbf{E_{4eq/eq}(O/O)}$ that already has two oxyl species at 1.5 V. Despite being slightly less stable (less than 0.06 eV), we considered $\mathbf{D_{4ax/eq}(O/OH)\text{-}B_{5ax}(O)}$ and $\mathbf{D_{4ax/eq}(O/OH)\text{-}C_{5eq}(O)}$ instead of $\mathbf{D_{4ax/eq}(OH/O)\text{-}B_{5ax}(O)}$ and $\mathbf{D_{4ax/eq}(OH/O)\text{-}C_{5eq}(O)}$, since the OER reaction can only take place when the oxyl group is in the axial site (see Supplementary material). We considered the I2M and the WNA mechanisms shown in Scheme 3.

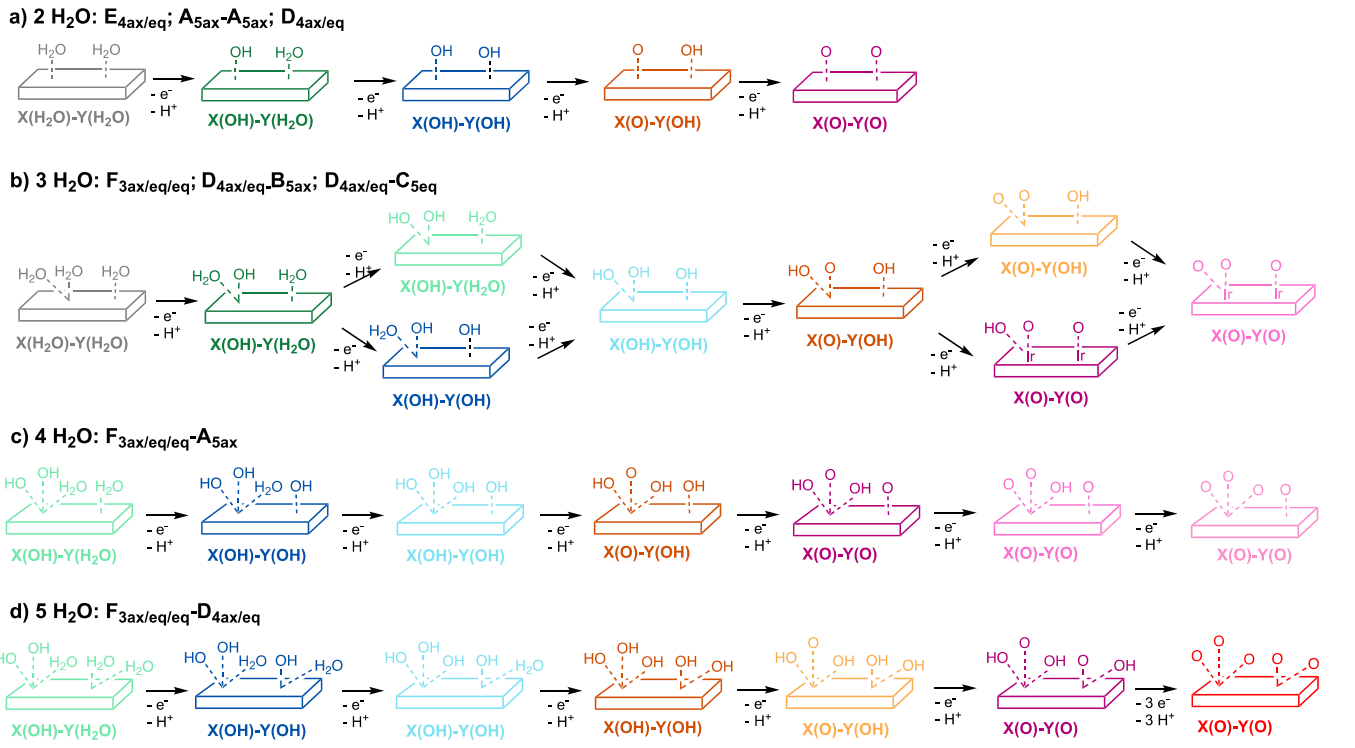

Scheme 2. Species considered for the H_2O oxidation at the different nanoparticle sites. Color labeling indicate the most oxidized species at each Ir center (See text for details).

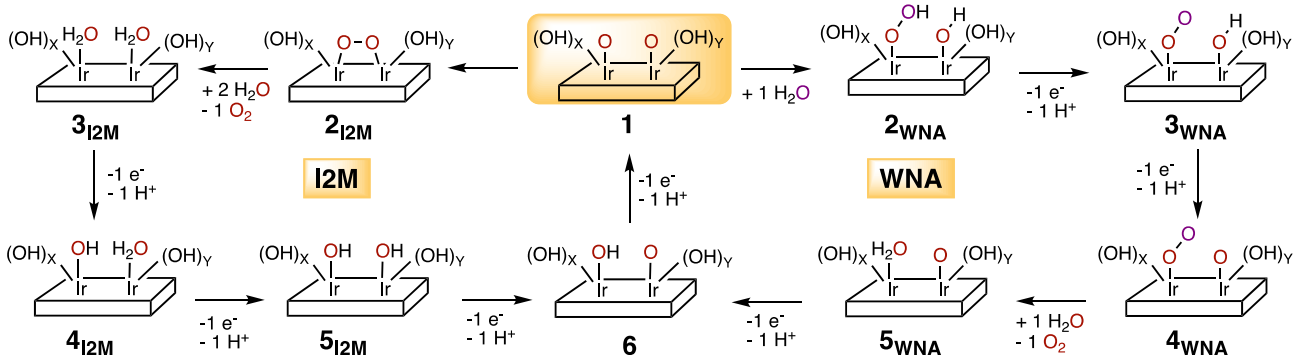

Scheme 3. Reaction mechanisms considered in this work.

Noteworthily, and similarly to the mechanistic proposal made by other authors[47,53,58] for the OER on the IrO_2 (110) surface, we decoupled the water attack in two steps: i) the splitting of water over two Ir-O groups (**1** to $\mathbf{2}_{WNA}$ process in Scheme 3) and ii) a PCET process from the Ir-OOH/Ir-OH species ($\mathbf{2}_{WNA}$ to $\mathbf{3}_{WNA}$). Nevertheless, and for comparison with the results reported in the literature,[56] the global reaction in which the water attack is coupled with the PCET has also been considered (see Table S18 of the supplementary material). Results show that the Ir-OOH/Ir-O species usually considered in the global reaction ($\mathbf{3'}_{WNA}$ in Scheme S1 of the supplementary material) is less stable than the Ir-OO/Ir-OH intermediate involved in the decoupled mechanism reported here, in agreement with previous results on surfaces.[48,53] Moreover, similar results are obtained for RuO_2 surfaces: the Ru-OO/Ru-OH intermediate is more stable than the Ru-OOH/Ru-O one and the geometrical features of the former matches with the experimental observations.[74] Therefore, it is very likely that regardless how the WNA process takes place (concerted or stepwise), the main intermediate involved in the O_2 formation is Ir-OO/Ir-OH rather than Ir-OOH/Ir-O. Comparison of the two approximations, assuming that the two routes involve the Ir-OO/Ir-OH species, suggests that the description of the WNA mechanism does not modify the general trends. Finally, since the two iridium centers are not equivalent in most of the pair of sites considered, there are two different WNA attack mechanisms depending on the iridium presenting the Ir-OOH species. We considered the two possibilities (WNA_X and WNA_Y in Scheme S2 of the supplementary material), the associated Gibbs energies for each pathway are reported in Table S18 and the optimized structures of all species considered in the OER processes are shown in Figures S10-S25 of the supplementary material. The values reported in the text correspond to the most favorable pathway for each pair of sites. The ΔG values for the individual steps are reported in Table 1 and Fig. 3 shows the global energy profile for the WNA mechanism.

The I2M mechanism starts with the coupling of two Ir-O species on the surface (**1** to $\mathbf{2_{I2M}}$ in Scheme 3 and Table 1). The process is in all cases endergonic, and the reaction Gibbs energies varies from 0.63 to 1.26 eV. These values tend to be slightly higher than those obtained with extended models,[48] although this may originate from the restrictions imposed for the optimizations with the nanoparticle models (See computational details). The energy cost for the O-O bond formation correlates reasonably well with the O···O distance in the initial structure (Table 1), since the more separated the oxygens initially are, the more unfavorable the process is. Moreover, we located the transition states for the oxo-coupling step involving $\mathbf{A_{5ax\text{-}A5ax}}$, $\mathbf{E_{4eq/eq}}$ and $\mathbf{F_{3ax/eq/eq\text{-}D4eq/ax}}$ sites as selected cases presenting very different environments. The computed energy barriers are in all cases large (>1.16 eV), thus suggesting that the oxo-coupling process is not only unfavorable, but also slow. In any case, after O-O bond formation, O_2 release by adsorption of two water molecules is thermodynamically favorable ($\Delta G°$ between −0.92 and −1.33 eV) in all sites except at $\mathbf{E_{4eq/eq}}$, where the reaction occurs in one single metal center. The catalytic cycle is closed through the oxidation of the adsorbed water species through processes that are equivalent to those described before and require potentials between 1.29 V and 1.58 V to recover the two Ir-O species. Overall, the I2M mechanism presents relatively low overpotentials (between 0.06 and 0.35 V). Indeed, these values are similar or even lower than those obtained for the WNA pathway (see below). However, the feasibility of the I2M mechanism is highly controlled by the oxo-coupling process, an endergonic chemical step with high energy barriers.

Table 1
Reaction Gibbs Energies (in eV) for the chemical and electrochemical steps of the I2M and WNA reaction mechanisms. Values in parenthesis correspond to the Gibbs energy barriers. For those sites including Ir centers of different nature, only the most favorable pathway is reported. Reaction conditions are 0 V potential versus SHE, pH = 0, T = 298 K and P = 1 atm.

Reaction	A_{5ax}-A_{5ax}	$E_{4eq/eq}$	$D_{4ax/eq}$-B_{5ax}	$D_{4ax/eq}$-C_{5eq}	$F_{3ax/eq/eq}$-A_{5ax}	$F_{3ax/eq/eq}$-$D_{4ax/eq}$
	I2M					
$\mathbf{1} \rightarrow \mathbf{2_{I2M}}$	0.81 (1.16)	0.80 (1.78)	0.63	1.02	1.17	1.26 (1.41)
$\mathbf{2_{I2M}} + 2\ H_2O \rightarrow \mathbf{3_{I2M}} + O_2$	−1.26	0.33	−0.92	−0.89	−0.36	−1.33
$\mathbf{3_{I2M}} \rightarrow \mathbf{4_{I2M}} + H^+ + e^-$	0.96	0.57	0.93	0.55	0.55	1.38
$\mathbf{4_{I2M}} \rightarrow \mathbf{5_{I2M}} + H^+ + e^-$	1.44	0.75	1.35	1.22	0.74	0.82
$\mathbf{5_{I2M}} \rightarrow \mathbf{6} + H^+ + e^-$	1.45	1.18	1.44	1.49	1.28	1.31
$\mathbf{6} \rightarrow \mathbf{1} + H^+ + e^-$	1.52	1.29	1.49	1.58	1.53	1.48
	WNA					
$\mathbf{1} + H_2O \rightarrow \mathbf{2_{WNA}}$	−0.53 (0.13)	0.47 (0.84)	−0.17	−0.27	0.09	−0.03 (0.43)
$\mathbf{2_{WNA}} \rightarrow \mathbf{3_{WNA}} + H^+ + e^-$	1.31	0.88	1.19	1.01	0.93	1.16
$\mathbf{3_{WNA}} \rightarrow \mathbf{4_{WNA}} + H^+ + e^-$	1.62	1.25	1.54	1.53	1.47	1.41
$\mathbf{4_{WNA}} + H_2O \rightarrow \mathbf{5_{WNA}} + O_2$	−0.40	0.47	−0.11	0.44	0.26	−0.09
$\mathbf{5_{WNA}} \rightarrow \mathbf{6} + H^+ + e^-$	1.40	0.56	0.99	0.68	0.83	0.99
$\mathbf{6} \rightarrow \mathbf{1} + H^+ + e^-$	1.52	1.29	1.48	1.52	1.34	1.48

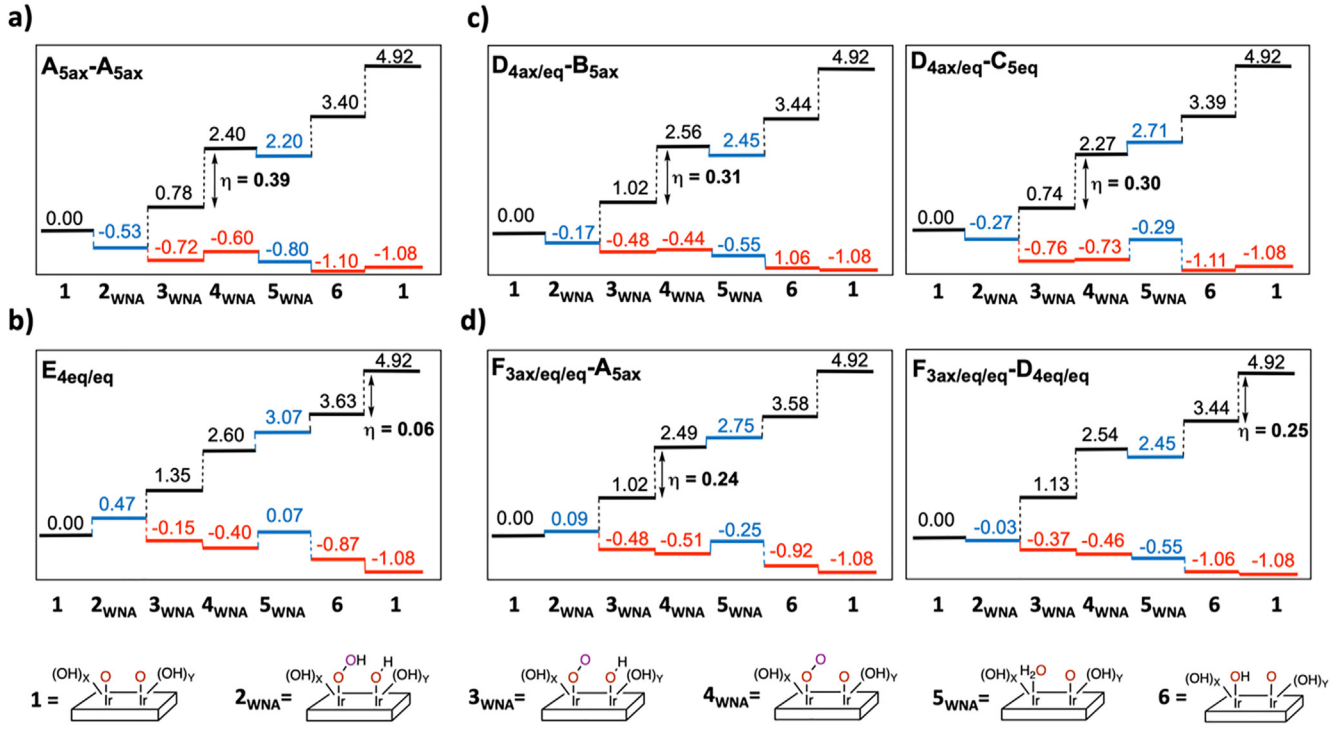

Fig. 3. Calculated Gibbs energy profile for the most favorable OER catalytic cycle through the WNA mechanism at: a) the reference (1 1 0) sites of the nanoparticle; b) the tip site of the nanoparticle; c) sites including one penta and one tetracoordinated metal center and d) sites including one tricoordinated site. The blue lines correspond to chemical steps, the black lines correspond to the energetics of the PCET at an applied potential of 0 V and the red values are for an applied potential of 1.5 V. Labelling taken from Fig. 1 and Scheme 3.

The WNA mechanism starts with the water attack to the two Ir-O of the surface, which leads to the formation of Ir-OOH and Ir-OH species (**1** to $\mathbf{2_{WNA}}$ in Scheme 3 and Table1). The reaction Gibbs energies for this step varies from −0.53 to 0.47 eV, but in most cases the process is essentially isergonic. In general, the reaction Gibbs energies for the WNA step at the different sites of the nanoparticle and the values obtained with extended surface models are very similar and they all suggest that the process is easy. The sole exception is the reaction at $\mathbf{E_{4eq/eq}}$. In this case, the process is unfavorable and the computed value (ΔG^o = 0.47 eV) is larger than that of the closely related (001) surface (ΔG^o = 0.25 eV). [48] Moreover, the computed Gibbs energy barriers for $\mathbf{A_{5ax}}$-$\mathbf{A_{5ax}}$, $\mathbf{E_{4eq/eq}}$ and $\mathbf{F_{3ax/eq/eq}}$-$\mathbf{D_{4ax/eq}}$ indicate that the process should be fast ($\Delta G^{\ddagger}$ less than 0.5 eV) with the exception for the $\mathbf{E_{4eq/eq}}$ tip site for which the transition state is 0.84 eV above the bisoxyl species + H_2-O. Remarkably, even for this $\mathbf{E_{4eq/eq}}$ site, the comparison between the WNA reaction Gibbs energy (0.47 eV) and the associated Gibbs energy barrier (0.84 eV) with those computed for the O-O bond formation in the I2M mechanism (0.80 eV and 1.78 eV, respectively) suggests that the WNA pathway is the preferred chemical step. Analysis of the spin densities over the oxygen atoms of Ir-O species (Table 2) shows that they have a marked oxyl radical character and thus, according to electronic density distribution, the water attack should be viewed as homolytic instead of nucleophilic. This is consistent with the fact that $\mathbf{E_{4eq/eq}}$ is the center presenting the lowest spin densities over the oxygen atoms.

After the O-O bond formation through the WNA mechanism, two PCET are required before O_2 is released ($\mathbf{2_{WNA}} \rightarrow \mathbf{3_{WNA}} + 1H^+ + 1e^-$ and $\mathbf{3_{WNA}} \rightarrow \mathbf{4_{WNA}} + 1H^+ + 1e^-$ in Scheme 3 and Table 1). For all centers, the $\mathbf{3_{WNA}}$ to $\mathbf{4_{WNA}}$ PCET is more challenging than the $\mathbf{2_{WNA}}$ to $\mathbf{3_{WNA}}$ one, the computed values being similar to those of the Ir-OH to Ir-O oxidation in the vicinity of a Ir-O group ($\mathbf{6} \rightarrow \mathbf{1} + H^+ + 1\ e^-$ step). Thus, the potential determining step involves in all cases a Ir-OH to Ir-O oxidation and depending on the site, this step is either the $\mathbf{3_{WNA}}$ to $\mathbf{4_{WNA}}$ oxidation or the **6** to **1** process (Scheme 3 and Tables 1 and S17). The resulting overpotentials are similar to those of the I2M pathway and range from 0.06 to 0.39 V.

Comparison between the O-O bond formation steps of the I2M and WNA mechanisms (Table 1) shows that the water attack is always more favorable than the oxo-coupling process. Moreover, the Gibbs energy barriers computed for some selected sites ($\mathbf{A_{5ax}}$-$\mathbf{A_{5ax}}$, $\mathbf{E_{4eq/eq}}$ and $\mathbf{F_{3ax/eq/eq}}$-$\mathbf{D_{4ax/eq}}$) show that the barriers are low for the WNA mechanism and significantly higher for the I2M pathway. Therefore, assuming a similar value for the other centers of the nanoparticle, the WNA seems to be the preferred route in all sites. Consequently, the analysis of the overpotentials required to perform the reaction in each site is made by comparing the values of the WNA mechanism.

Fig. 3 summarizes the Gibbs energies of the most favorable WNA pathway for the 6 different sites of the nanoparticle. It also reports the required overpotentials (η^{OER}) and outlines the potential determining step. The Figure is divided in four groups. $\mathbf{A_{5ax}}$-$\mathbf{A_{5ax}}$ site, which corresponds to two iridium centers on the most stable (110) surface and thus, its reactivity is taken as the reference value (Fig. 3a). The energetics associated with $\mathbf{E_{4eq/eq}}$, which is the sole site involving only one iridium center, is shown in Fig. 3b and those of all other sites, organized according to the coordination number of the least saturated site, are given in Fig. 3c for tetracoordinated metals and in Fig. 3d for tricoordinated species. The computed overpotentials vary from 0.06 V to 0.39 V and they are mostly between 0.24 and 0.39 V. The differences are less than 0.15 eV, and fall within the DFT accuracy. However, since errors due to the level of theory are likely to be similar for all sites, trends are expected to be properly described. Indeed, the computed overpotential for the reference $\mathbf{A_{5ax}}$-$\mathbf{A_{5ax}}$ site corresponds to the highest value (0.39 V), suggesting that most of the sites of the nanoparticle would be more reactive than the sites on the most stable (110) surface in agreement with the higher activity found for nanoparticles.[22,26,27] The case of $\mathbf{E_{4eq/eq}}$ is special: it presents the lowest overpotential (only 0.06 V) but the corresponding chemical processes are unfavorable and present high energy barriers. This seems to be detrimental in the final catalytic activity. Indeed, the experimentally reported Tafel plots show almost not activity at potentials below 1.4 V,[26,75,76] which would be consistent with the fact that this site is not active. Noteworthily, the overpotentials computed for sites including one tetracoordinated metal as the least saturated center ($\mathbf{D_{4ax/eq}}$-$\mathbf{B_{ax}}$ and $\mathbf{D_{4ax/eq}}$-$\mathbf{C_{eq}}$, Fig. 3c) are larger than those computed for sites including initially tricoordinated iridium atoms ($\mathbf{F_{3ax/eq/eq}}$-$\mathbf{A_{5ax}}$ and $\mathbf{F_{3ax/eq/eq}}$-$\mathbf{D_{4ax/eq}}$, Fig. 3d) by 0.05 – 0.07 eV. The two groups show overpotentials that are lower to those of the $\mathbf{A_{5ax}}$-$\mathbf{A_{5ax}}$ site of the (110) facet. Despite the differences are small and fall within the accuracy of the computational approach, this is indicative that initially low coordinated sites would be more active. Unfortunately, according to Alexandrov and co-workers,[46] these Ir-OH containing species are likely less stable and would readily dissolve in acidic conditions. This would correlate with the number of surface OH groups at reaction conditions. Indeed, at working conditions it is expected that all vacant sites will be saturated with adsorbed species and according to the required overpotentials for the Iridium oxidation, these will mostly be OH groups. Therefore, the tricoordinated metals would present two OH groups on the surface and the tetracoordinated species one single OH. Overall, our results seem to suggest that the highest activity of IrO_2 nanoparticles when compared with crystalline materials and particularly the (110) facet arise both by the increase of active sites per mass of catalyst and the higher activity of low coordinated sites. Remarkably, these low coordinated centers are likely more abundant on non-crystalline materials, thus suggesting that this could be one of the key factors for the highest activity of amorphous materials and, particularly, nanoparticles.[24,26,30].

Table 2
Ir-O_L distances (in Å) and spin moment for the most stable structures at working potentials.

Species	Ir_1-O_{11}	Ir_1-O_{12}	Ir_1-O_{13}	Ir_2-O_{21}	Ir_2-O_{22}	O_1-O_2[a]	S_{O1}[b]	S_{O2}[c]	S_{Ir1}	S_{Ir2}
$\mathbf{A_O}$-$\mathbf{A_O}$	1.805			1.808		3.067	0.626	0.640	0.533	0.527
$\mathbf{E_{O/O}}$	1.772	1.770			–	2.900	0.233/0.255		0.406	
$\mathbf{D_{OH/O}}$	1.941	1.794			N/A		0.582		0.565	
$\mathbf{D_{O/OH}}$-$\mathbf{B_O}$	1.772	1.934		1.796		2. 889	0.441	0.471	0.240	0.281
$\mathbf{D_{O/OH}}$-$\mathbf{C_O}$	1.939	1.794		1.950	1.804	4.434	0.587	0.698	0.582	0.532
$\mathbf{F_{O/OH/OH}}$	1.778	1.917	1.930	1.804			0.314		0.314	
$\mathbf{F_{O/OH/OH}}$-$\mathbf{A_O}$-	1.776	1.916	1.931	1.787		3.249	0.412	0.646	0.389	0.538
$\mathbf{F_{O/OH/OH}}$-$\mathbf{D_{OH/O}}$	1.768	1.927	1.921	1.804		3.234	0.692	−0.242	0.700	−0.239

[a] Distance between oxygens involved in the oxo-coupling step.
[b] Oxygen atom of the Ir-O species at Ir_1.
[c] Oxygen atom of the Ir-O species at Ir_2.

4. Conclusions

Calculations on the oxygen evolution reaction catalytic activity of several iridium sites present on the $(IrO_2)_{33}$ Wulff-like stoichiometric nanoparticle model show that pentacoordinated sites located at the (1 1 0) surface are slightly less active when compared to other centers of the nanoparticle. In contrast, tri- and tetracoodinated sites mainly located at tip, corner or edges (in larger models) of the nanoparticle present lower overpotentials. Despite the computed differences are small and may fall within the modeling approach accuracy, present work suggests that using nanoparticles instead of films has two main advantages. On one side, the use of nanoparticles increases the number of active sites per mass of catalyst and, on the other side, nanoparticles present low coordinated sites at corners and edges that would be more active than sites found in crystalline facets. These low coordinated sites are not fully oxidized at potentials around 1.5 V and the most stable structure at reaction conditions is $Ir(O)(OH)_X$ (X = 1 or 2 for tetra- or tricoordinated centers, respectively). These low coordinated sites are likely more abundant in amorphous materials, which could be one of the factors contributing to the higher catalytic activity of amorphous materials.

Declaration of Competing Interest

The authors declare that they have no known competing financial interests or personal relationships that could have appeared to influence the work reported in this paper.

Acknowledgement

This work was supported by the Ministerio de Ciencia e Innovación, SpainGeneralitat de Catalunya, Spain, MICINN [CTQ2017-89132-P and PID2020-112715GB-I00], the Generalitat de Catalunya [2017SGR1323] and Red Española de Supercomputación [QCM-2019-1-0043, QS-2019-2-0031].

Appendix A. Supplementary data

Supplementary data to this article can be found online at https://doi.org/10.1016/j.jcat.2022.05.023.

References

[1] L. Hammarström, Acc. Chem. Res. 42 (2009) 1859–1860.
[2] S. Anantharaj, V. Aravindan, Adv. Energy Mater. 10 (2020) 1902666.
[3] M.G. Walter, E.L. Warren, J.R. McKone, S.W. Boettcher, Q. Mi, E.A. Santori, N.S. Lewis, Chem. Rev. 110 (2010) 6446–6473.
[4] X. Sala, S. Maji, R. Bofill, J. García-Antón, L. Escriche, A. Llobet, Acc. Chem. Res. 47 (2014) 504–516.
[5] J.D. Blakemore, R.H. Crabtree, G.W. Brudvig, Chem. Rev. 115 (2015) 12974–13005.
[6] B.M. Hunter, H.B. Gray, A.M. Müller, Chem. Rev. 116 (2016) 14120–14136.
[7] J.H. Montoya, L.C. Seitz, P. Chakthranont, A. Vojvodic, T.F. Jaramillo, J.K. Nørskov, Nat. Mater. 16 (2017) 70–81.
[8] C. Spöri, J.T.H. Kwan, A. Bonakdarpour, D.P. Wilkinson, P. Strasser, Angew. Chemie Int. Ed. 56 (2017) 5994–6021.
[9] H. Ding, H. Liu, W. Chu, C. Wu, Y. Xie, Chem. Rev. 121 (2021) 13174–13212.
[10] E. Fabbri, A. Habereder, K. Waltar, R. Kötz, T.J. Schmidt, Catal, Sci. Technol. 4 (2014) 3800–3821.
[11] T. Reier, H.N. Nong, D. Teschner, R. Schlögl, P. Strasser, Adv. Energy Mater. 7 (2017) 1601275.
[12] L. An, C. Wei, M. Lu, H. Liu, Y. Chen, G.G. Scherer, A.C. Fisher, P. Xi, Z.J. Xu, C. Yan, Adv. Mater. 33 (2021) 2006328.
[13] C.C.L. McCrory, S. Jung, I.M. Ferrer, S.M. Chatman, J.C. Peters, T.F. Jaramillo, J. Am. Chem. Soc. 137 (2015) 4347–4357.
[14] J. Yu, Q. He, G. Yang, W. Zhou, Z. Shao, M. Ni, ACS Catal. 9 (2019) 9973–10011.
[15] D. Lebedev, R. Ezhov, J. Heras-Domingo, A. Comas-Vives, N. Kaeffer, M. Willinger, X. Solans-Monfort, X. Huang, Y. Pushkar, C. Copéret, A.C.S. Cent, Sci. 6 (2020) 1189–1198.
[16] J. Cheng, J. Yang, S. Kitano, G. Juhasz, M. Higashi, M. Sadakiyo, K. Kato, S. Yoshioka, T. Sugiyama, M. Yamauchi, N. Nakashima, ACS Catal. 9 (2019) 6974–6986.
[17] H.N. Nong, T. Reier, H.-S. Oh, M. Gliech, P. Paciok, T.H.T. Vu, D. Teschner, M. Heggen, V. Petkov, R. Schlögl, T. Jones, P. Strasser, Nat. Catal. 1 (2018) 841–851.
[18] D. Böhm, M. Beetz, M. Schuster, K. Peters, A.G. Hufnagel, M. Döblinger, B. Böller, T. Bein, D. Fattakhova-Rohlfing, Adv. Funct. Mater. 30 (2020) 1906670.
[19] Q. Wang, Z. Zhang, C. Cai, M. Wang, Z.L. Zhao, M. Li, X. Huang, S. Han, H. Zhou, Z. Feng, L. Li, J. Li, H. Xu, J.S. Francisco, M. Gu, J. Am. Chem. Soc. 143 (2021) 13605–13615.
[20] M. Ledendecker, S. Geiger, K. Hengge, J. Lim, S. Cherevko, A.M. Mingers, D. Göhl, G.V. Fortunato, D. Jalalpoor, F. Schüth, C. Scheu, K.J.J. Mayrhofer, Nano Res. 12 (2019) 2275–2280.
[21] Y. Zhao, E.A. Hernandez-Pagan, N.M. Vargas-Barbosa, J.L. Dysart, T.E. Mallouk, J. Phys. Chem. Lett. 2 (2011) 402–406.
[22] T. Reier, M. Oezaslan, P. Strasser, ACS Catal. 2 (2012) 1765–1772.
[23] H. Jiang, S. Ge, Y. Zhang, M. Dong, S. Wu, M. Wu, J. Zhang, R. Ge, Z. Guo, J. Phys. Chem. C 124 (2020) 2–8.
[24] P. Jovanovič, N. Hodnik, F. Ruiz-Zepeda, I. Arčon, B. Jozinović, M. Zorko, M. Bele, M. Šala, V.S. Šelih, S. Hočevar, M. Gaberšček, J. Am. Chem. Soc. 139 (2017) 12837–12846.
[25] R.M. Kluge, R.W. Haid, A.S. Bandarenka, J. Catal. 396 (2021) 14–22.
[26] D.F. Abbott, D. Lebedev, K. Waltar, M. Povia, M. Nachtegaal, E. Fabbri, C. Copéret, T.J. Schmidt, Chem. Mater. 28 (2016) 6591–6604.
[27] Y. Lee, J. Suntivich, K.J. May, E.E. Perry, Y. Shao-Horn, J. Phys. Chem. Lett. 3 (2012) 399–404.
[28] P. Lettenmeier, L. Wang, U. Golla-Schindler, P. Gazdzicki, N.A. Cañas, M. Handl, R. Hiesgen, S.S. Hosseiny, A.S. Gago, K.A. Friedrich, Angew. Chemie Int. Ed. 55 (2016) 742–746.
[29] L. Fu, X. Zeng, C. Huang, P. Cai, G. Cheng, W. Luo, Inorg. Chem. Front. 5 (2018) 1121–1125.
[30] E. Oakton, D. Lebedev, M. Povia, D.F. Abbott, E. Fabbri, A. Fedorov, M. Nachtegaal, C. Copéret, T.J. Schmidt, ACS Catal. 7 (2017) 2346–2352.
[31] R. Badam, M. Hara, H.-H. Huang, M. Yoshimura, Int. J. Hydrogen Energy 43 (2018) 18095–18104.
[32] F. Bizzotto, J. Quinson, A. Zana, J.J.K. Kirkensgaard, A. Dworzak, M. Oezaslan, M. Arenz, Catal, Sci. Technol. 9 (2019) 6345–6356.
[33] D. Lebedev, C. Copéret, A.C.S. Appl, Energy Mater. 2 (2019) 196–200.
[34] H. Dau, C. Limberg, T. Reier, M. Risch, S. Roggan, P. Strasser, ChemCatChem 2 (2010) 724–761.
[35] E. Fabbri, T.J. Schmidt, ACS Catal. 8 (2018) 9765–9774.
[36] S. Divanis, T. Kutlusoy, I.M. Ingmer Boye, I.C. Man, J. Rossmeisl, Chem. Sci. 11 (2020) 2943–2950.
[37] O. Piqué, F. Illas, F. Calle-Vallejo, Phys. Chem. Chem. Phys. 22 (2020) 6797–6803.
[38] K.A. Stoerzinger, O. Diaz-Morales, M. Kolb, R.R. Rao, R. Frydendal, L. Qiao, X.R. Wang, N.B. Halck, J. Rossmeisl, H.A. Hansen, T. Vegge, I.E.L. Stephens, M.T.M. Koper, Y. Shao-Horn, ACS Energy Lett. 2 (2017) 876–881.
[39] M. García-Melchor, L. Vilella, N. López, A. Vojvodic, ChemCatChem 8 (2016) 1792–1798.
[40] K. Klyukin, A. Zagalskaya, V. Alexandrov, J. Phys. Chem. C 122 (2018) 29350–29358.
[41] L.C. Seitz, C.F. Dickens, K. Nishio, Y. Hikita, J. Montoya, A. Doyle, C. Kirk, A. Vojvodic, H.Y. Hwang, J.K. Norskov, T.F. Jaramillo, Science 353 (2016) 1011–1014.
[42] G. Buvat, M.J. Eslamibidgoli, A.H. Youssef, S. Garbarino, A. Ruediger, M. Eikerling, D. Guay, ACS Catal. 10 (2020) 806–817.
[43] J. Gao, C.-Q. Xu, S.-F. Hung, W. Liu, W. Cai, Z. Zeng, C. Jia, H.M. Chen, H. Xiao, J. Li, Y. Huang, B. Liu, J. Am. Chem. Soc. 141 (2019) 3014–3023.
[44] W. Sun, Z. Wang, W.Q. Zaman, Z. Zhou, L. Cao, X.-Q. Gong, J. Yang, Chem. Commun. 54 (2018) 996–999.
[45] J. Rossmeisl, Z.-W. Qu, H. Zhu, G.-J. Kroes, J.K. Nørskov, J. Electroanal. Chem. 607 (2007) 83–89.
[46] A. Zagalskaya, V. Alexandrov, J. Phys. Chem. Lett. 11 (2020) 2695–2700.
[47] H.N. Nong, L.J. Falling, A. Bergmann, M. Klingenhof, H.P. Tran, C. Spöri, R. Mom, J. Timoshenko, G. Zichittella, A. Knop-Gericke, S. Piccinin, J. Pérez-Ramírez, B.R. Cuenya, R. Schlögl, P. Strasser, D. Teschner, T.E. Jones, Nature 587 (2020) 408–413.
[48] D. González, J. Heras-Domingo, M. Sodupe, L. Rodríguez-Santiago, X. Solans-Monfort, J. Catal. 396 (2021) 192–201.
[49] Z. Xu, J. Rossmeisl, J.R. Kitchin, J. Phys. Chem. C 119 (2015) 4827–4833.
[50] S. Siahrostami, A. Vojvodic, J. Phys. Chem. C 119 (2015) 1032–1037.
[51] I.C. Man, H. Su, F. Calle-Vallejo, H.A. Hansen, J.I. Martínez, N.G. Inoglu, J. Kitchin, T.F. Jaramillo, J.K. Nørskov, J. Rossmeisl, ChemCatChem 3 (2011) 1159–1165.
[52] Y.-H. Fang, Z.-P. Liu, J. Am. Chem. Soc. 132 (2010) 18214–18222.
[53] Y. Ping, R.J. Nielsen, W.A. Goddard, J. Am. Chem. Soc. 139 (2017) 149–155.
[54] J.A. Gauthier, C.F. Dickens, L.D. Chen, A.D. Doyle, J.K. Nørskov, J. Phys. Chem. C 121 (2017) 11455–11463.
[55] L.G.V. Briquet, M. Sarwar, J. Mugo, G. Jones, F. Calle-Vallejo, ChemCatChem 9 (2017) 1261–1268.
[56] C.F. Dickens, C. Kirk, J.K. Nørskov, J. Phys. Chem. C 123 (2019) 18960–18977.
[57] A. Halder, C. Liu, Z. Liu, J.D. Emery, M.J. Pellin, L.A. Curtiss, P. Zapol, S. Vajda, A. B.F. Martinson, J. Phys. Chem. C 122 (2018) 9965–9972.

[58] K. Bhattacharyya, C. Poidevin, A.A. Auer, J. Phys. Chem. C 125 (2021) 4379–4390.
[59] D. González, B. Camino, J. Heras-Domingo, A. Rimola, L. Rodríguez-Santiago, X. Solans-Monfort, M. Sodupe, J. Phys. Chem. C 124 (2020) 1227–1237.
[60] D. González, J. Heras-Domingo, S. Pantaleone, A. Rimola, L. Rodríguez-Santiago, X. Solans-Monfort, M. Sodupe, ACS Omega 4 (2019) 2989–2999.
[61] D. González, M. Sodupe, L. Rodríguez-Santiago, X. Solans-Monfort, Nanoscale 13 (2021) 14480–14489.
[62] G. Kresse, J. Furthmüller, Phys. Rev. B 54 (1996) 11169–11186.
[63] G. Kresse, J. Hafner, Phys. Rev. B 47 (1993) 558–561.
[64] J.P. Perdew, K. Burke, M. Ernzerhof, Phys. Rev. Lett. 77 (1996) 3865–3868.
[65] S. Grimme, J. Comput. Chem. 25 (2004) 1463–1473.
[66] Y. Ping, G. Galli, W.A. Goddard, J. Phys. Chem. C 119 (2015) 11570–11577.
[67] X. Solans-Monfort, V. Branchadell, M. Sodupe, M. Sierka, J. Sauer, J. Chem. Phys. 121 (2004) 6034–6041.
[68] G. Kresse, D. Joubert, Phys. Rev. B 59 (1999) 1758–1775.
[69] P.E. Blöchl, Phys. Rev. B 50 (1994) 17953–17979.
[70] K. Mathew, R. Sundararaman, K. Letchworth-Weaver, T.A. Arias, R.G. Hennig, J. Chem. Phys. 140 (2014) 084106.
[71] H.H. Heenen, J.A. Gauthier, H.H. Kristoffersen, T. Ludwig, K. Chan, J. Chem. Phys. 152 (2020) 144703.
[72] J.K. Nørskov, J. Rossmeisl, A. Logadottir, L. Lindqvist, J.R. Kitchin, T. Bligaard, H. Jónsson, J. Phys. Chem. B 108 (2004) 17886–17892.
[73] H.N. Nong, L. Gan, E. Willinger, D. Teschner, P. Strasser, Chem. Sci. 5 (2014) 2955–2963.
[74] R.R. Rao, M.J. Kolb, L. Giordano, A.F. Pedersen, Y. Katayama, J. Hwang, A. Mehta, H. You, J.R. Lunger, H. Zhou, N.B. Halck, T. Vegge, I. Chorkendorff, I.E.L. Stephens, Y. Shao-Horn, Nat. Catal. 3 (2020) 516–525.
[75] K.A. Stoerzinger, L. Qiao, M.D. Biegalski, Y. Shao-Horn, J. Phys. Chem. Lett. 5 (2014) 1636–1641.
[76] M. Kan, X. Qian, T. Zhang, D. Yue, Y. Zhao, A.C.S. Sustain, Chem. Eng. 5 (2017) 10940–10946.